

Recrystallization or cooling ages: *in situ* UV-laser $^{40}\text{Ar}/^{39}\text{Ar}$ geochronology of muscovite in mylonitic rocks

ANDREAS MULCH & MICHAEL A. COSCA

Institut de Minéralogie et Géochimie, Université de Lausanne, BFSH-2, CH-1015 Lausanne, Switzerland

(e-mail: andreas.mulch@img.unil.ch)

Abstract: The intra-grain $^{40}\text{Ar}/^{39}\text{Ar}$ age distributions of muscovite from greenschist-facies mylonite zones are shown to be sensors of metamorphic history. Textures, compositions and *in situ* UV-laser ablation $^{40}\text{Ar}/^{39}\text{Ar}$ data from two extensional shear zones demonstrate that cooling ages can be distinguished from neo- or recrystallization ages. Deformed muscovite porphyroclasts and recrystallized shear band muscovite from the Pogallo Shear Zone (Ivrea Zone, southern Alps) reveal variable intra-grain $^{40}\text{Ar}/^{39}\text{Ar}$ ages with internal age variations of more than 65 Ma. The wide range of $^{40}\text{Ar}/^{39}\text{Ar}$ ages within compositionally homogeneous grains is consistent with diffusion-dominated argon loss controlled by observable intra-grain microstructures. In contrast, intra-grain $^{40}\text{Ar}/^{39}\text{Ar}$ ages of muscovite fish from Proterozoic mylonite of the Porsgrunn–Kristiansand Shear Zone (Southern Norway) display only minor age dispersion, and age variations are correlated with changes in muscovite composition. The sympathetic age–composition correlations in different muscovite microstructures directly relate to sequential neo- and recrystallization of muscovite and ultimately provide insight into the protracted recrystallization history during extensional deformation along the Porsgrunn–Kristiansand Shear Zone.

Keywords: absolute age, argon, muscovite, diffusion, recrystallization.

Mylonite zones are commonly characterized by intense localization of ductile shear and represent exhumed zones of deformation in the middle and lower crust (e.g. Tullis *et al.* 1982; Schmid & Handy 1991). Geological and geophysical evidence indicates that mylonite zones are extensions of shallow-level brittle faults at depth and accommodate deformation at scales as large as the entire lithosphere (e.g. Sibson 1986). Numerous attempts have been made to quantify the timing of deformation within shear zones using a variety of dating techniques (e.g. Costa & Maluski 1988; Dunlap *et al.* 1991; Mezger *et al.* 1991; Getty & Gromet 1992; West & Lux 1993; Freeman *et al.* 1997; Müller *et al.* 2000*b*; Sherlock & Hetzel 2001; Mulch *et al.* 2002*c*). However, only in rare cases can a clear distinction between cooling, recrystallization and neocrystallization ages be made and the ultimate significance of the geochronological data often remains equivocal. Isotopic exchange in recrystallized minerals is controlled by the relative importance of microstructure development involving grain-size reduction (Goodwin & Renne 1991), neo- and recrystallization (Kirschner *et al.* 1996; Dunlap 1997), formation of intra-grain microfractures (Mulch *et al.* 2002*b*), and isotope loss by diffusion (e.g. Hames & Bowring 1994). Insight into the complex relationship between cooling ages and ages of neo- and recrystallization within mylonitic rocks can be gained from Kirschner *et al.* (1996). Their study of argon retention in micrometre-sized white mica in the basal thrust of an Alpine fold and thrust nappe provides an excellent example of how neocrystallized mica can be used to reconstruct the deformation history of low-temperature mylonites. On the basis of thermometric and biostratigraphic constraints, Kirschner *et al.* (1996) argued that staircase-shaped step-heating $^{40}\text{Ar}/^{39}\text{Ar}$ spectra from foliation-parallel white mica within the mylonite are inconsistent with available data for argon diffusion in muscovite and do not reflect predicted intra-grain argon loss profiles. Rather, their results demonstrate that the staircase spectra record a *c.* 15 Ma time interval of muscovite growth during protracted ductile deformation. Similarly, Dunlap (1997) placed time constraints on thrust-related mylonitic deformation within the

Ruby Gap duplex (Australia) using bulk step-heating $^{40}\text{Ar}/^{39}\text{Ar}$ data and microstructural characterization to distinguish between an (inherited) old white mica component and muscovite that neocrystallized during formation of the duplex. Despite the success of these studies, difficulties arise when the mechanisms of isotopic exchange in structurally and compositionally heterogeneous minerals have to be assessed from bulk mineral data. Consequently, new developments in geochronology have been directed towards the use of texturally controlled *in situ* dating of minerals, and a state-of-the-art review of approaches undertaken within different disciplines of geochronology has been given by Müller (2003).

In situ UV-laser $^{40}\text{Ar}/^{39}\text{Ar}$ dating circumvents some of the problems associated with geochronological analyses of bulk mineral separates, as data can be obtained from well-defined areas within individual grains that can be characterized on a microstructural and microchemical basis. In addition to its high spatial resolution (e.g. Kelley *et al.* 1994; Giorgis *et al.* 2000; Kelley & Wartho 2000; Kramar *et al.* 2001; Reddy *et al.* 2001; Mulch *et al.* 2002*b*), UV-laser $^{40}\text{Ar}/^{39}\text{Ar}$ geochronology provides a powerful dating tool for fabric-forming white mica in greenschist-facies mylonites. This paper presents *in situ* UV-laser $^{40}\text{Ar}/^{39}\text{Ar}$ geochronological, microstructural and microchemical analyses of muscovite from two greenschist-facies extensional mylonite zones and compares the effects of microstructure development, neo- and recrystallization and diffusive argon loss on intra-grain $^{40}\text{Ar}/^{39}\text{Ar}$ patterns. In particular, we propose that texturally and compositionally controlled *in situ* UV-laser $^{40}\text{Ar}/^{39}\text{Ar}$ dating can be used to successfully distinguish between cooling and neo- or recrystallization ages within mylonitic rocks.

Synkinematic neo- and recrystallization and exchange of radiogenic ^{40}Ar in white mica

White mica can grow under a variety of metamorphic conditions and over variable time scales. Consequently, white mica popula-

tions and even individual grains may represent compositionally and isotopically heterogeneous systems. This is even more critical in mylonitic rocks deformed under brittle or viscous conditions because parameters controlling isotopic exchange such as recrystallization rate, cooling rate and interaction with syntectonic fluids can vary considerably during the evolution of mylonite zones.

Diffusive argon exchange: the 'high-temperature' side of $^{40}\text{Ar}/^{39}\text{Ar}$ geochronology

At elevated temperatures diffusion of argon is the dominant process controlling the accumulation of argon within a crystal. It is beyond the scope of this paper to explore the details of argon diffusion in minerals and the interested reader is referred to the study by McDougall & Harrison (1999). However, the widespread application of $^{40}\text{Ar}/^{39}\text{Ar}$ thermochronology to decipher relative movements across shear zones using a suite of K-bearing minerals that are characterized by a 'prescribed closure temperature' and subsequent inversion of the $^{40}\text{Ar}/^{39}\text{Ar}$ data into points in temperature–time space warrants some remarks about thermochronology in deformed rocks.

Numerous thermochronological studies adopt the mathematical formulation of a 'closure temperature' by Dodson (1973). Crucial to interpretations of closure temperatures are assumptions regarding cooling rate and diffusion length scale, a variable often assumed to be the grain size of the respective mineral. An increasing number of laser $^{40}\text{Ar}/^{39}\text{Ar}$ studies on argon isotope zoning (e.g. Phillips & Onstott 1988; Scaillet *et al.* 1990; Hodges *et al.* 1994) suggest that thermally activated volume diffusion of radiogenic argon in micas occurs within the K-interlayer parallel to the (001) cleavage plane and is best described by a cylindrical diffusion geometry (e.g. Giletti 1974; Harrison *et al.* 1985). In the simplest case the effective diffusion length scale in micas equals the half-diameter of the basal plane (e.g. Hames & Bowring 1994). However, there is growing evidence from natural samples that effective diffusion length scales can be considerably smaller than the physical grain size (e.g. Harrison *et al.* 1985; Goodwin & Renne 1991; Wright *et al.* 1991; Kramar *et al.* 2001). In mylonitic rocks, the effect of syn- to post-kinematic grain coarsening (as a result of grain boundary migration or annealing) or grain-size reduction caused by synkinematic neo- and recrystallization may greatly complicate the mathematical formulation and the straightforward application of an isotopic closure temperature. The effects of grain-size reduction on $^{40}\text{Ar}/^{39}\text{Ar}$ ages have been addressed by a series of furnace step-heating studies (e.g. Goodwin & Renne 1991; Cosca *et al.* 1992; Hess *et al.* 1993; West & Lux 1993; Dunlap 1997; Markley *et al.* 2002). Goodwin & Renne (1991) demonstrated that thermal resetting of biotite during mylonitization and grain-size reduction is reflected in decreasing apparent ages with decreasing grain size, a phenomenon that is most readily explained in terms of argon loss by thermally activated volume diffusion on different length scales. Recent, *in situ* laser $^{40}\text{Ar}/^{39}\text{Ar}$ geochronological studies (Hames & Cheney 1997; Kramar *et al.* 2001; Mulch *et al.* 2002b) have documented that diffusion of radiogenic argon in naturally deformed mica does not necessarily occur on the grain scale. Indeed, argon diffusion in deformed micas appears to be strongly controlled by the presence and distribution of lattice-modifying microstructures, such as high-angle kink bands, dislocation networks and (micro-)fractures, that serve as high-diffusivity pathways (Kramar *et al.* 2003). Although it is common in thermochronological studies to assign a specific isotopic closure temperature to a suite of minerals, it is obvious

from the above considerations that there is no unique 'closure temperature' for any particular mineral. More generally, these considerations highlight the need for complete microstructural and microchemical sample characterization when interpreting $^{40}\text{Ar}/^{39}\text{Ar}$ data from strongly deformed metamorphic rocks.

Reaction, neo- and recrystallization: $^{40}\text{Ar}/^{39}\text{Ar}$ exchange at 'low temperatures'

Many minerals used for $^{40}\text{Ar}/^{39}\text{Ar}$ geochronology (e.g. feldspar, mica and amphibole) have solid solutions and their compositions are continually modified in response to changes in pressure, temperature and fluid composition during deformation and metamorphism. It is no surprise to see in the published literature numerous examples that demonstrate the isotopic and compositional heterogeneity of white mica from rocks deformed under low- and intermediate-temperature conditions. This heterogeneity is reflected in irregular $^{40}\text{Ar}/^{39}\text{Ar}$ step-heating spectra (e.g. Scaillet *et al.* 1990; Jaboyedoff & Cosca 1999) and is attributed to dating mixtures of several generations of white mica (Wijbrans & McDougall 1986), recrystallization and contemporaneous diffusive argon loss (West & Lux 1993) or neocrystallization (Kirschner *et al.* 1996; Dunlap 1997). Spatially resolved geochronology of compositional growth zoning in metamorphic garnet (e.g. Christensen *et al.* 1988; Vance & O'Nions 1990) or strain fringes around pyrite clasts (Müller *et al.* 2000a) has considerably furthered our understanding of the rates and time scales of metamorphic processes. In a similar fashion, we can apply *in situ* $^{40}\text{Ar}/^{39}\text{Ar}$ geochronology to date different generations of synkinematic muscovite once the relative recrystallization and growth histories have been established.

Recrystallization in micas is mainly accommodated by basal dislocation glide within the K-interlayer (e.g. Banos *et al.* 1983; Mares & Kronenberg 1993). Additionally, formation of kink band boundaries and/or microfractures (e.g. Bell *et al.* 1986; Goodwin & Wenk 1990; Shea & Kronenberg 1992; Mares & Kronenberg 1993), and dilation along the basal cleavage plane (e.g. Goodwin & Wenk 1990) are common in naturally deformed micas. Because of the inert nature of argon, the fraction and inter-connectivity of defect sites in the lattice, where the relatively large argon atom can be hosted, effectively control its intra-lattice migration (Lee 1995). All of the above-mentioned deformation mechanisms potentially introduce and promote migration of these lattice defects and increase their inter-connectivity. Strain-induced recrystallization by defect migration thus has the highest potential for providing recrystallization ages because the reconstitution of crystalline material allows rapid synkinematic isotopic exchange with an external reservoir.

$^{40}\text{Ar}/^{39}\text{Ar}$ geochronology and the role of fluids in shear zones

One factor often vaguely invoked to explain variations in $^{40}\text{Ar}/^{39}\text{Ar}$ data is the presence of fluids. Because mylonitic shear zones represent prime candidates for enhanced fluid flow, the interaction with syn- and post-tectonic fluids can potentially influence $^{40}\text{Ar}/^{39}\text{Ar}$ ages either by introducing a component of excess ^{40}Ar or by alteration of the mineral assemblage. Whereas mineral alteration or neocrystallization of secondary minerals can be identified by electron microprobe analysis (EMPA) or laser-ablation inductively coupled plasma mass spectrometry (LA-ICP-MS), in many cases the detection of excess argon is not straightforward. Commonly, middle- to upper-crustal extensional shear zones can be regarded as open systems where the fluid

'residence' times are particularly short and fluid flow is dominated by low-salinity, low- $\delta^{18}\text{O}$ meteoric fluids (e.g. Morrison & Anderson 1998). To maintain their $\delta^{18}\text{O}$ composition, infiltration of these fluids must occur without significant isotopic exchange between the fluid and the fault rock. Consequently, these fluids and resulting fluid inclusions within the mineral of interest should maintain a $^{40}\text{Ar}/^{36}\text{Ar}$ ratio that is close to the $^{40}\text{Ar}/^{36}\text{Ar}$ ratio of the atmosphere and is commonly corrected for in $^{40}\text{Ar}/^{39}\text{Ar}$ geochronology. Furthermore, argon is a highly incompatible element in the mica-water system and will partition strongly into the fluid phase (Kelley 2002). Thus, the amounts of excess ^{40}Ar introduced into the mineral by interaction with meteoric fluids are presumably small compared with the overall (radiogenic) ^{40}Ar contribution (Kelley 2002). Even though excess argon has been shown to be a potential pitfall in dating deformed metamorphic rocks (e.g. Reddy *et al.* 1996; Müller 2003), high spatial resolution, *in situ* UV-laser dating has the highest potential to detect excess argon within the mineral.

In general, recrystallization and reaction processes will play a significant role at temperatures lower than those necessary for significant argon diffusion, but are secondary to diffusive argon loss within high-temperature deformation regimes where elevated temperatures outlast the deformation event. Infiltration of meteoric fluids within extensional shear zones potentially promotes hydration reactions and associated neocrystallization of mineral phases, but given the relatively low argon mica-fluid partition coefficients, will introduce only minor modifications of $^{40}\text{Ar}/^{39}\text{Ar}$ ages as a result of excess argon. The following two examples, from extensional mylonite zones with entirely different thermal histories, document the disparate $^{40}\text{Ar}/^{39}\text{Ar}$ data that can be obtained from similar tectonic settings and how these data can be resolved using *in situ* UV-laser $^{40}\text{Ar}/^{39}\text{Ar}$ geochronology.

Example 1: *in situ* UV-laser $^{40}\text{Ar}/^{39}\text{Ar}$ geochronology of muscovite from the Pogallo Shear Zone (Ivrea Zone, southern Alps, Italy)

The Pogallo Shear Zone is a zone of oblique mylonitic shear that accommodated exhumation of deep and intermediate crustal rocks of the southern Alpine basement. Mylonitization occurred under retrograde amphibolite- to greenschist-facies conditions (Handy 1987). The Pogallo mylonites overprint Early Permian mafic dykes (Mulch *et al.* 2002c) and granitoids, but are themselves truncated by brittle faults related to Tertiary Alpine tectonics (Handy 1987). Correlating the temperatures of syntectonic, retrograde metamorphism within the Pogallo Shear Zone (500–300 °C) with the cooling curve for the southern Ivrea Zone yields a broad age range of 170–220 Ma for the timing of mylonitization (Handy & Zingg 1991). A detailed *in situ* UV-laser $^{40}\text{Ar}/^{39}\text{Ar}$ study of three microstructurally distinct muscovite types from micaceous mylonite of the Pogallo Shear Zone reveals highly variable apparent ages within deformed muscovite porphyroclasts and muscovite situated within extensional shear bands. In contrast, undeformed muscovite porphyroclasts when analysed by furnace step heating are characterized by a flat age spectrum (Mulch *et al.* 2002b). Individual deformed muscovite porphyroclasts display radiogenic argon loss of up to 40% and apparent ages that are >65 Ma younger than the results of step-heating experiments from undeformed porphyroclasts (Fig. 1a). Similarly, the $^{40}\text{Ar}/^{39}\text{Ar}$ spectrum obtained from these deformed porphyroclasts forms a staircase-shaped spectrum with apparent ages rising from 85.7 ± 1.4 Ma to 180.6 ± 2.6 Ma (errors are reported as 2σ throughout) nearly identical to the range of ages (116.8 ± 7.4 Ma to 189.5 ± 11.1 Ma) measured by *in situ* UV-laser $^{40}\text{Ar}/^{39}\text{Ar}$ dating (Mulch *et al.* 2002b). *In situ* UV-laser

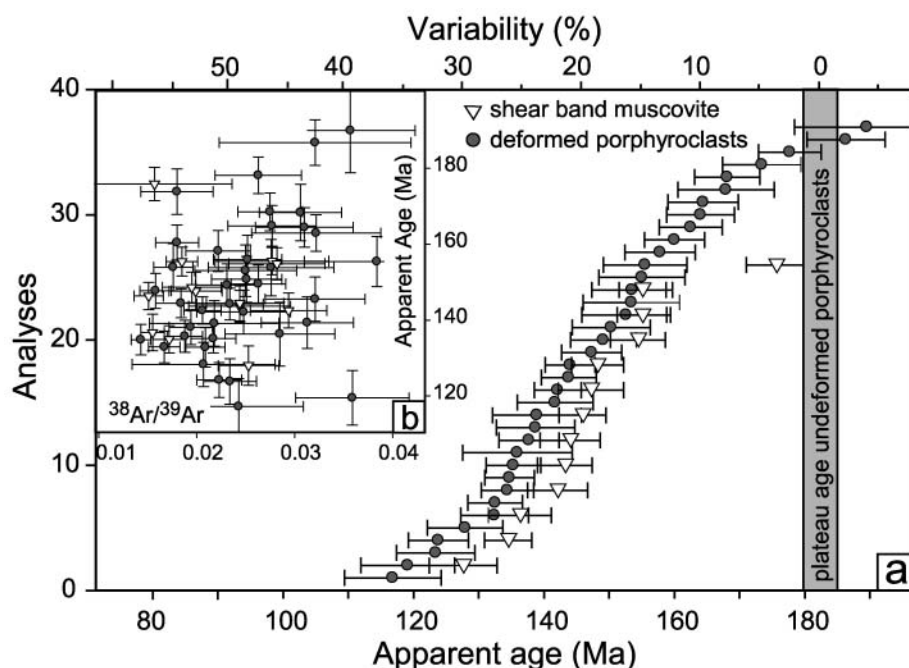


Fig. 1. (a) Cumulative graph of *in situ* UV-laser $^{40}\text{Ar}/^{39}\text{Ar}$ ages from muscovite of the Pogallo Shear Zone. Strongly deformed muscovite porphyroclasts and shear band muscovite display ages consistent with significant argon loss. Undeformed muscovite porphyroclasts yield a step-heating plateau age of 182.0 ± 2.0 Ma. As expected for diffusional argon loss, the oldest *in situ* $^{40}\text{Ar}/^{39}\text{Ar}$ ages overlap, within error, with the age of the undeformed grains. Errors given are 2σ . The full dataset and analytical details have been given by Mulch *et al.* (2002b). (b) $^{38}\text{Ar}/^{39}\text{Ar}$ isotopic correlation plot. Shear band muscovite grains occupy a very restricted $^{38}\text{Ar}/^{39}\text{Ar}$ range consistent with compositional and isotopic homogeneity. Plot symbols are the same for (a) and (b).

ablation $^{40}\text{Ar}/^{39}\text{Ar}$ data for muscovite in the extensional shear bands exhibit the same behaviour, with intra-grain apparent ages covering a range from 127.6 ± 5.2 Ma to 175.4 ± 4.4 Ma (Fig. 1a). In contrast to laser studies of argon concentration gradients within undeformed white mica (e.g. Hames & Bowring 1994; Hodges *et al.* 1994), the distribution of $^{40}\text{Ar}/^{39}\text{Ar}$ apparent ages in muscovite analysed within a plane parallel to the mylonitic lineation and perpendicular to the foliation of the mylonite does not follow a grain-scale volume diffusion pattern. The observation of similar apparent age ranges recorded in millimetre-sized deformed porphyroclasts and considerably smaller shear band micas suggests that both muscovite types share a common mechanism for argon loss and that argon loss occurred on variable length scales.

The presence of early kinematic, fibrolitic sillimanite in the Pogallo mylonite (Fig. 2) indicates that amphibolite-facies conditions prevailed during the onset of mylonitization. Initial deformation temperatures (≥ 550 °C) were well above the closure temperature for muscovite and the mylonite cooled during extension-related exhumation, thus following a $T-t$ evolution similar to the model assumptions described by Dodson (1973). On the basis of the observed heterogeneously spaced lattice-modifying microstructures such as high-angle kink bands, zones of high dislocation density and microfractures, Mulch *et al.* (2002b) concluded that diffusive argon loss was occurring from microstructurally controlled segments over length scales defined by the orientation and spacing of the observed microstructures. Consequently, the effective diffusion dimensions are highly variable and can be smaller than the laser pit size of 60 μm used in this study.

One way to test whether the variation of *in situ* $^{40}\text{Ar}/^{39}\text{Ar}$ ages

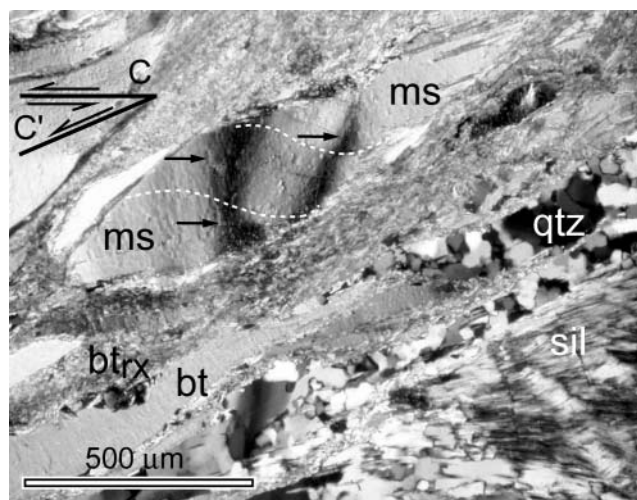


Fig. 2. Photomicrograph (cross-polarized light) of deformed muscovite next to greenschist-facies extensional shear band (lower left) in mylonite from the Pogallo Shear Zone. Deformation of the muscovite porphyroclasts results in folding of basal cleavage (dotted white lines) and segmentation of muscovite by high-angle kinks and microfractures (black arrows). Spacing and size of segmentation can vary from tens to several hundred microns within individual grains. Early kinematic (relict) fibrolitic sillimanite (lower right) is deformed by the greenschist-facies extensional shear band consistent with cooling of the mylonite from amphibolite- to greenschist-facies conditions during extensional shearing and uplift. ms, muscovite; bt, biotite; qtz, quartz; sil, fibrolitic sillimanite; btr, recrystallized biotite in C' -type shear band.

in muscovite from the Pogallo mylonite reflects diffusional loss from heterogeneously sized segments or localized recrystallization of sequentially younger segments is to compare the age–composition relationships of porphyroclasts and shear band muscovite. The shear band muscovite and deformed porphyroclasts do not reveal any significant intra- and inter-grain compositional variation with respect to $(\text{Mg} + \text{Fe}_{\text{tot}})$, ^{IV}Al and ^{VI}Al when subjected to EMPA and plot close to the muscovite end-member composition (Fig. 3a). However, shear band muscovite reveals significantly lower Ti contents (< 0.06 per formula unit, p.f.u.) compared with the porphyroclasts (Fig. 3b). The Ti content in some metamorphic white mica has been linked to metamorphic grade with a steady increase from about 0.02 p.f.u. in greenschist-facies rocks to about 0.12 p.f.u. under amphibolite-facies conditions (450–700 °C; Guidotti, 1986). Given the existence of a Ti-saturating phase such as rutile, the Ti content of metamorphic micas in Al-rich rocks should be at the saturation limit for P and T during formation and can therefore be qualitatively correlated with metamorphic grade (Guidotti, 1986). The lower Ti content of the shear band muscovite therefore supports a model of falling temperature during shear band formation consistent with decreasing $P-T$ during greenschist-facies extensional mylonitization and uplift of Pogallo footwall mylonite (e.g. Handy 1987). No evidence has been found for fluid-mediated alteration associated with synkinematic recrystallization of the shear band muscovite, either within the very fine-grained recrystallized biotite or around the pre-existing muscovite porphyroclasts. Isotope correlation plots can potentially be used in $^{40}\text{Ar}/^{39}\text{Ar}$ geochronology to detect the presence or absence of composition–age correlations. We have used the $^{38}\text{Ar}/^{39}\text{Ar}$ ratio to verify if chlorine-derived ^{38}Ar exerts an influence on the *in situ* UV-laser $^{40}\text{Ar}/^{39}\text{Ar}$ ages. As already documented for major elements by EMPA, both muscovite types from the Pogallo mylonite are fairly homogeneous; however, the $^{38}\text{Ar}/^{39}\text{Ar}$ ratios of deformed muscovite porphyroclasts ($^{38}\text{Ar}/^{39}\text{Ar} = 0.0143\text{--}0.0384$), when plotted against apparent age, show a larger variation compared with undeformed porphyroclasts ($^{38}\text{Ar}/^{39}\text{Ar}$ of plateau-forming steps is 0.0131–0.0183) and recrystallized shear band muscovite ($^{38}\text{Ar}/^{39}\text{Ar} = 0.0151\text{--}0.0282$) (Fig. 1b). The smaller internal $^{38}\text{Ar}/^{39}\text{Ar}$ variation of recrystallized shear band muscovite compared with deformed porphyroclasts suggests greater compositional and isotopic homogeneity. The wealth of compositional data demonstrates that although muscovite porphyroclasts and shear band muscovite are homogeneous on the intra-grain scale, their mineral compositions are clearly discernible. This observation suggests that the shear band muscovite recrystallized during deformation and that the composition of the recrystallized grains adjusted to synkinematic changes in $P-T-X$ during deformation and uplift of the mylonite. Therefore, the identical intra-grain $^{40}\text{Ar}/^{39}\text{Ar}$ age pattern of both temporally and compositionally distinct mica types renders any interpretation of the $^{40}\text{Ar}/^{39}\text{Ar}$ data based on localized recrystallization unlikely. In contrast, tremendous intra-grain age variations within compositionally homogeneous grains are much more consistent with temperature-controlled diffusive argon loss and lend strong support to the viability of a model of post-kinematic diffusive argon loss at the segment scale.

Example 2: *in situ* UV-laser $^{40}\text{Ar}/^{39}\text{Ar}$ geochronology of syntectonic muscovite from the Porsgrunn–Kristiansand Shear Zone (Southern Norway)

Retrograde mylonite exposed at the Proterozoic Porsgrunn–Kristiansand Shear Zone (Southern Norway) contains muscovite

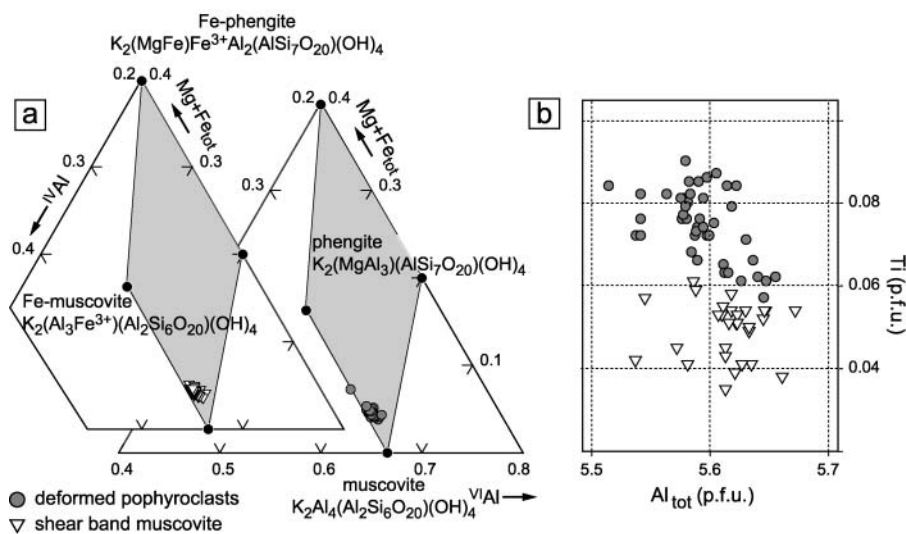


Fig. 3. (a) Ternary composition plots for deformed muscovite porphyroclasts and shear band muscovite from the Pogallo Shear Zone. Both muscovite types plot close to the muscovite end-member component and do not show significant variations in major elements. (b) In contrast, lower Ti contents in shear band muscovite are consistent with recrystallization during decreasing metamorphic conditions.

within the mylonitic foliation and muscovite fish that are oblique to the foliation and commonly associated with chlorite-bearing extensional shear bands in the hanging wall of the extensional mylonite zone (Fig. 4). On the basis of detailed mapping of the Porsgrunn–Kristiansand Shear Zone, its structural position and kinematics, the mylonites can be shown to have accommodated extensional reactivation of an earlier high-grade metamorphic (Sveconorwegian/Grenvillian; *c.* 1.1–1.2 Ga) mylonitic fabric. The hanging-wall mylonite consists of an interconnected muscovite and chlorite network within a quartz-rich matrix. Muscovite defines the mylonitic C-foliation or forms mica fish oblique to the mylonitic foliation. Synkinematic chlorite trails commonly extend from the terminations of the oblique muscovite fish into the mylonitic foliation or into extensional (C') shear bands (Fig. 4). These shear bands indicate an overall top-to-the-SE sense of shear consistent with the sense of shear deduced from the orientation of muscovite fish, the asymmetry of K-feldspar porphyroclasts, and associated growth of synkinematic chlorite within the porphyroclast pressure shadows. Synkinematic growth of muscovite is inferred from its spatial and kinematic association with chlorite in the extensional shear bands and in the pressure shadows of the muscovite fish (Figs 4 and 5), as well as from oxygen isotope data, consistent with neocrystallization from low- $\delta^{18}\text{O}$ meteoric fluids ($\delta^{18}\text{O}_{\text{ms}} = 0.15\text{--}0.40\text{‰}$ relative to SMOW). In contrast to the Pogallo example where syntectonic temperatures slowly fell from amphibolite- to greenschist-facies conditions, deformation within the Porsgrunn–Kristiansand Shear Zone occurred close to the brittle–viscous transition in quartz-rich, phyllosilicate-bearing rocks. Evidence comes from numerous quartz-filled fractures that crosscut the mylonitic foliation but recrystallized during deformation. The mutual transition from brittle failure to viscous flow of quartz in these veins is thought to reflect synkinematic changes in strain rate and/or fluid pressure at temperatures slightly above those necessary for crystal plastic deformation in quartz (*c.* 300 °C, Masuda *et al.* 1997). Deformation modes within the Porsgrunn–Kristiansand Shear Zone mylonite most probably switched between brittle failure (vein formation) and viscous flow (recrystallization of the veins) and the rocks stayed within the lower greenschist facies over a prolonged period of time. Altogether the available data indicate that the observed microstructures are likely to record the same deformation event and that mylonitic deformation occurred under lower greenschist-facies conditions

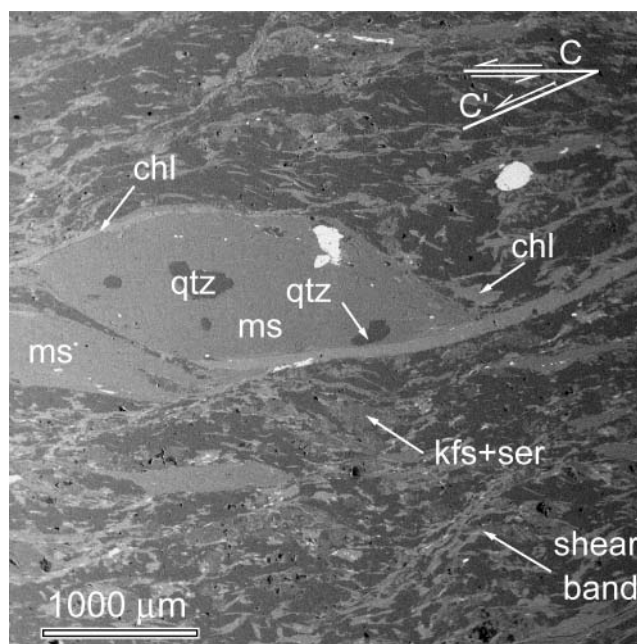
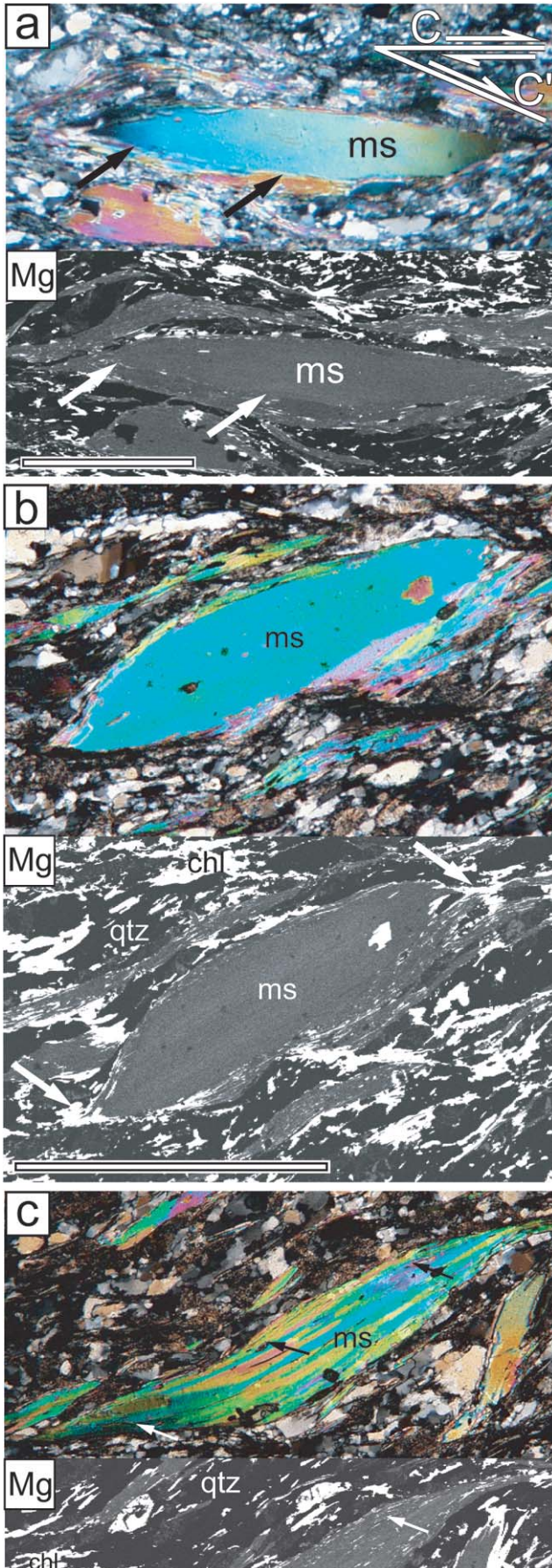


Fig. 4. Backscattered-electron image of synkinematic high-Al muscovite fish in mylonite from the Porsgrunn–Kristiansand Shear Zone. Chlorite occurs in the mylonitic C-foliation, in C' shear bands, and in pressure shadows of muscovite fish. Sense of shear is sinistral (top-to-the-SE) as deduced from orientation of C' shear bands (upper right to lower left) and the asymmetry of the oblique muscovite fish.

($T = 300 \pm 50^\circ\text{C}$), consistent with the results of oxygen isotope thermometry in the footwall and hanging wall of the shear zone (Mulch *et al.* 2002a).

Three types of muscovite are investigated in this study: (1) foliation-parallel low-Al muscovite that displays a recrystallized high-Al rim; (2) oblique, high-Al muscovite fish; (3) muscovite fish composed of individual muscovite 'sub'grains (Fig. 5). In contrast to the deformed muscovite porphyroclasts of the Pogallo example, both the recrystallized high-Al muscovite fish and composite muscovite exhibit a typical sigmoidal grain shape with their long axes rotated antithetically to the mylonitic (C-)foliation



(Fig. 5b and c). Foliation-parallel muscovite has lower Al and higher Ti contents compared with the recrystallized muscovite fish. As shown in Figure 5a some of this low-Al muscovite reveals recrystallized muscovite grains along its grain boundaries with the same high-Al and low-Ti signature as the high-Al muscovite fish, consistent with a common recrystallization history for the small muscovite grains and the high-Al muscovite fish.

In situ UV-laser $^{40}\text{Ar}/^{39}\text{Ar}$ data from foliation-forming, low-Al ($Al_{\text{tot}} < 5.3 \text{ p.f.u.}$) muscovite

Foliation-forming low-Al muscovite has remarkably homogeneous intra-grain $^{40}\text{Ar}/^{39}\text{Ar}$ ages with only a very small degree (<3%) of variability (Figs 6a and 7a). Individual analyses generally overlap within error (Table 1) and apparent ages range from 879 ± 15 to 894 ± 12 Ma (Fig. 6a). There is no systematic trend in apparent age when approaching the edge of the mica (the high-Al rims could not be analysed within this grain).

In situ UV-laser ablation $^{40}\text{Ar}/^{39}\text{Ar}$ data from high-Al ($Al_{\text{tot}} > 5.3 \text{ p.f.u.}$) muscovite fish

High-Al muscovite occurs as oblique muscovite fish commonly bound by chlorite-bearing extensional shear bands. The high-Al muscovite fish can be composed of (sub)grains usually measuring several hundreds of microns parallel to (001) and some tens of microns across (001), but commonly represent optically continuous millimetre-sized muscovite grains (Fig. 5b). No fine-grained recrystallized muscovite was observed in thin section. EMPA revealed total Al contents generally around 5.45 p.f.u., and these high-Al muscovite fish display a range of apparent ages from 864 ± 14 Ma to 891 ± 18 Ma (Fig. 6b and d). The ages do not correlate with distance to the grain boundaries parallel to (001) and there is no evidence for the formation of diffusion profiles over the scale of the muscovite fish. The weighted mean of apparent ages recorded in the high-Al muscovite fish (880.2 ± 5.5 Ma; MSWD = 1.30) is within error of the weighted mean of foliation-forming, low-Al muscovite (888.0 ± 4.0 Ma; MSWD = 0.60). The two weighted mean ages are statistically indistinguishable, thereby precluding any distinction regarding the relative timing of neo- and recrystallization in low-Al and high-Al muscovite. The slightly younger weighted mean age and a larger scatter in apparent ages may be geologically meaningful and reflect a larger age range recorded within the recrystallized high-Al muscovite fish. Microstructural observations indicate that

Fig. 5. Microstructures of (a) foliation-parallel low-Al muscovite, (b) recrystallized high-Al muscovite fish, and (c) composite muscovite fish from the Porsgrunn–Kristiansand Shear Zone. (a) Photomicrograph of foliation-forming muscovite displaying a rim of recrystallized muscovite (arrows) around undeformed muscovite core. X-ray map of Mg distribution within the same grain shows clear-cut core–rim boundary (white arrows) and the absence of magnesium zoning within the core. (b) Recrystallized, high-Al muscovite fish and X-ray map of Mg distribution. High-Al muscovite fish have the same composition as small, recrystallized muscovite grains at the margins of the muscovite fish. The presence of synkinematic chlorite in the pressure shadows of the muscovite fish (white arrows) should be noted. (c) Composite muscovite fish showing heterogeneously sized (sub)grains that vary in composition (different grey shades in X-ray map of Mg distribution). Composite muscovite fish commonly show numerous chlorite intergrowths (white arrows). Cross-polarized light in (a)–(c). Scale bars represent 1 mm.

high-Al muscovite fish postdate crystallization and growth of the foliation-forming, low-Al muscovite; however, more high-spatial resolution $^{40}\text{Ar}/^{39}\text{Ar}$ data are needed to confirm or dismiss such a hypothesis. Similar to the example from the Pogallo Shear Zone, microstructurally distinct muscovite grains have contrasting Ti contents (Fig. 6d). The overall decrease in Ti and the spatial and kinematic association of the oblique muscovite fish with the chlorite in the extensional shear bands are consistent with formation under decreasing P and falling T , and point to

synkinematic recrystallization of the oblique muscovite fish during protracted deformation in the mylonite zone.

In situ UV-laser ablation $^{40}\text{Ar}/^{39}\text{Ar}$ data from composite muscovite fish

Composite muscovite fish represent aggregates of numerous variably sized (tens to hundreds of micrometres) fish-shaped muscovite (sub)grains (Fig. 5c). These muscovite (sub)grains have variable composition and cover the entire compositional range encompassing the fields of the foliation-parallel, low-Al muscovite and the recrystallized high-Al muscovite fish (Fig. 6d). Composite muscovite fish have very similar microstructures compared with some of the high-Al muscovite fish, but their compositional heterogeneity indicates only localized recrystallization of individual muscovite (sub)grains, rather than crystal-scale recrystallization. The intra-grain $^{40}\text{Ar}/^{39}\text{Ar}$ ages cover the complete age range of 862 ± 24 Ma to 910 ± 11 Ma (Fig. 7a) measured in the other muscovite types from this study. The observed age distribution of these composite muscovite grains thus displays the highest variability (weighted mean age 889 ± 12 Ma; MSWD = 3.90) consistent with their variable composition. Chlorine-derived ^{38}Ar is a less useful tracer for the different muscovite types found within detachment mylonite of the Porsgrunn–Kristiansand Shear Zone, and compositional changes during recrystallization are much more obvious in elements such as Ti, Ba, and Sr that show systematic enrichment (Ba, Sr) or depletion (Ti) in the recrystallized muscovite. High Cl-derived ^{38}Ar contents frequently reflect Cl-rich fluid inclusions enriched in extraneous argon (McDougall & Harrison 1999). The $^{38}\text{Ar}/^{39}\text{Ar}$ of all three muscovite types, however, overlaps within error and exhibits similar scatter (Fig. 7b). It is thus unlikely that the marked variability in $^{40}\text{Ar}/^{39}\text{Ar}$ ages of the different muscovite types can be attributed to extraneous argon in fluid inclusions or to varying amounts of ^{39}Ar -recoil, a phenomenon common in samples that contain fine-scale, fluid inclusion rich intergrowths of chlorite (Lo & Onstott 1989).

The three microstructurally and compositionally distinct muscovite types analysed from the Porsgrunn–Kristiansand Shear Zone reveal a consistent age–composition correlation. Whereas the foliation-parallel, low-Al muscovite grains yield a restricted range of $^{40}\text{Ar}/^{39}\text{Ar}$ ages (879–894 Ma), the age range recorded in the recrystallized, high-Al muscovite fish is consistently younger (864–891 Ma), or in the case of the composite partially recrystallized muscovite fish there is much more age dispersion

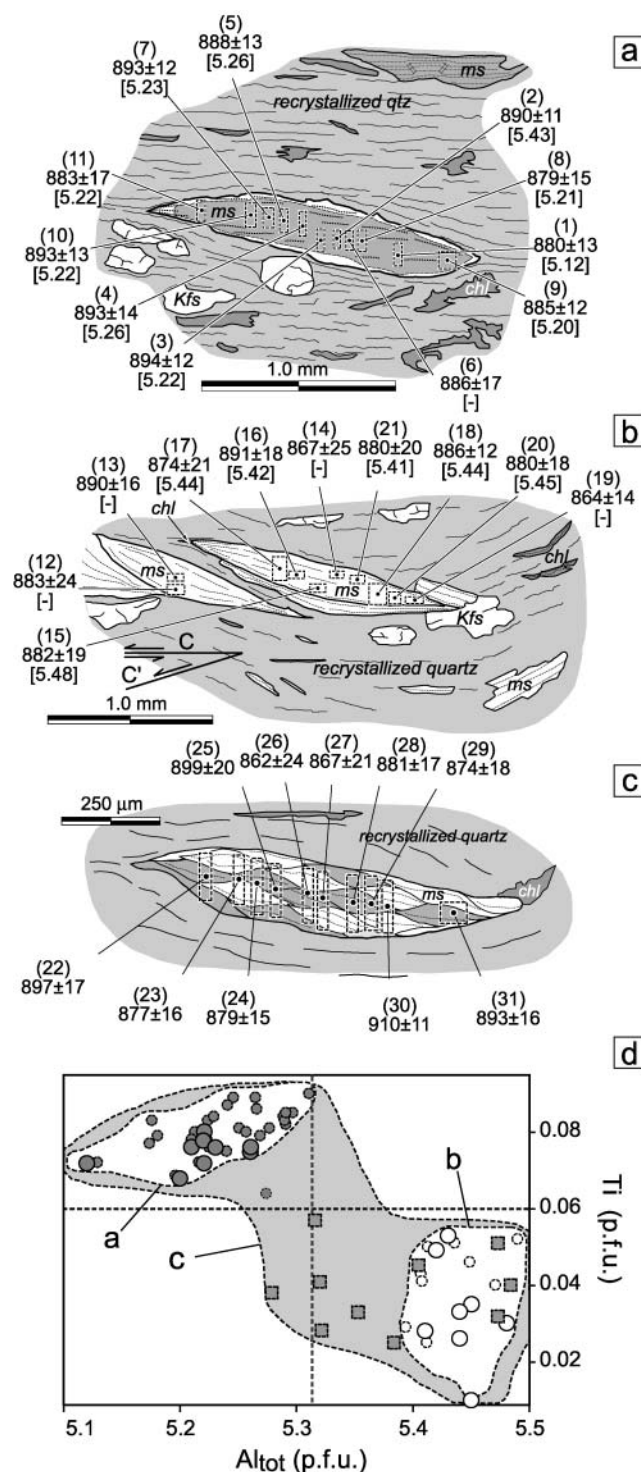


Fig. 6. Line drawing showing the distribution of *in situ* UV-laser ablation $^{40}\text{Ar}/^{39}\text{Ar}$ ages and the total Al and Ti contents in high- and low-Al muscovite and composite muscovite fish as detected by EMPA. (a) Foliation-parallel muscovite with low-Al core (grey) and recrystallized high-Al rim (white). (b) High-Al (white) oblique muscovite fish shown by chlorite-bearing shear bands. (c) Composite muscovite fish as shown in Figure 5c. Composite fish consist of individual muscovite sub-grains (drawn schematically) that range in composition between the low-Al (grey) and the high-Al (white) muscovite. It should be noted that individual laser spots sample different muscovite sub-grains. (d) Compositional variation of low-Al muscovite, high-Al muscovite fish, and composite muscovite fish (grey shaded field). Filled symbols represent composition measured at individual laser spots shown in (a)–(c); small symbols represent additional analyses from the same grains. ms, muscovite; Kfs, K-feldspar; chl, chlorite; qtz, quartz. Errors given are 2σ . Numbers in parentheses refer to analysis labels in Table 1. Square brackets indicate total Al per formula unit.

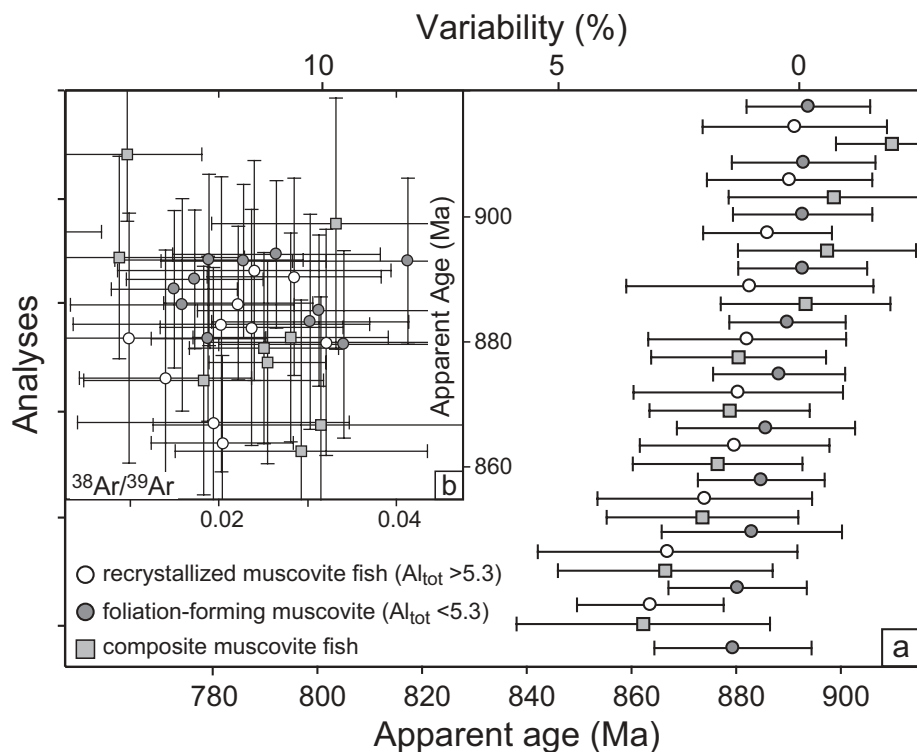


Fig. 7. (a) Cumulative plot of intra- and inter-grain variation of *in situ* UV-laser ages in muscovite from Porsgrunn–Kristiansand Shear Zone mylonite. Intra-grain variations for low-Al (●) and high-Al (○) muscovite are small and overlap within error. Composite muscovite fish (grey squares) cover the entire range of ages recorded by the high- and low-Al muscovite. Errors given are 2σ . (b) $^{38}\text{Ar}/^{39}\text{Ar}$ correlation plot. The $^{38}\text{Ar}/^{39}\text{Ar}$ ratios of different muscovite types overlap within error and show no $^{38}\text{Ar}/^{39}\text{Ar}$ –age correlation thus eliminating fine-scale Cl-rich intergrowths and associated ^{39}Ar recoil or extraneous argon in fluid inclusions as a possible source for the scatter in the $^{40}\text{Ar}/^{39}\text{Ar}$ ages. Plot symbols are the same for (a) and (b).

(862–909 Ma) (Fig. 7a). The same range of ages recorded within composite muscovite fish with a (sub) grain size of about 50–200 μm and significantly large (millimetre-sized) low-Al muscovite argues against significant diffusive Ar loss within muscovite from the Porsgrunn–Kristiansand Shear Zone. On the basis of their oxygen isotopic signature ($\delta^{18}\text{O}_{\text{ms}} = 0.15\text{--}0.40\text{‰}$ relative to SMOW), foliation-parallel low-Al muscovite neocrystallized from syntectonic meteoric fluids that infiltrated the shear zone during the extension event. There is no evidence from *in situ* UV-laser and furnace step-heating data for the presence of extraneous argon owing to syntectonic fluids. Microstructures and oxygen isotope thermometry data (*c.* 300 $^{\circ}\text{C}$), and the grain size uncorrelated with $^{40}\text{Ar}/^{39}\text{Ar}$ intra-grain age patterns, are consistent with lower greenschist facies deformation temperatures, thus excluding a significant influence of diffusion-controlled argon loss. On the basis of the microstructural observations, the results from oxygen isotope thermometry and the similarity of *in situ* $^{40}\text{Ar}/^{39}\text{Ar}$ data, we suggest that the sympathetic age–composition correlation directly relates to sequential neo- and recrystallization of muscovite during extensional deformation along the Porsgrunn–Kristiansand Shear Zone.

Conclusions

(1) Compositional changes during recrystallization in nature and experiment have been documented for a variety of minerals including amphibole (Stünitz 1998), plagioclase (Yund & Tullis 1991), phlogopite (Etheridge & Hobbs 1974) and biotite (Goodwin & Renne 1991). Together with microfabric analyses, they provide a reliable guide for distinguishing synkinematically recrystallized from non-recrystallized grains. Both examples presented in this study show microstructurally distinct muscovite types that display compositional differences in minor and trace

elements. However, given a similar structural context the pattern of *in situ* $^{40}\text{Ar}/^{39}\text{Ar}$ apparent ages differs strongly between the two examples, thus suggesting different mechanisms for loss or retention of radiogenic argon within white mica.

(2) Highly variable intra-grain $^{40}\text{Ar}/^{39}\text{Ar}$ ages with internal variations of more than 65 Ma within deformed muscovite porphyroclasts and recrystallized shear band muscovite from the Pogallo Shear Zone are inconsistent with localized recrystallization and diffusive argon loss on the grain scale. Given the microstructural and compositional evidence, they rather record diffusion of argon on the scale of microstructurally controlled segments and subsequent fast pathway diffusion along first-order lattice discontinuities.

(3) The homogeneous distribution of intra-grain $^{40}\text{Ar}/^{39}\text{Ar}$ apparent ages for muscovite from the Porsgrunn–Kristiansand Shear Zone strongly contrasts with the widespread $^{40}\text{Ar}/^{39}\text{Ar}$ age scatter within muscovite of the Pogallo example. Given the relatively low deformation temperatures and the stable isotope evidence that the foliation-forming low-Al muscovite neocrystallized syntectonically in the presence of meteoric fluids, the *in situ* $^{40}\text{Ar}/^{39}\text{Ar}$ data from the different muscovite microstructures can be interpreted to directly date neo- and recrystallization of muscovite in the shear zone.

(4) The results of this study suggest that using texturally controlled, $^{40}\text{Ar}/^{39}\text{Ar}$ *in situ* UV-laser geochronology, a distinction between cooling ages and ages of neo- and recrystallization can be made provided recrystallized microstructures in muscovite can be discerned based on microstructural and compositional criteria and the intra-grain age–composition relationships can be established.

This study was supported by the Swiss National Science Foundation (SNF grants 2000-056849 and 20-65025.01). We would like to thank A. Andresen, M. R. Handy and N. Kramar for comments and helpful discussions during

Table 1. In situ UV-laser $^{40}\text{Ar}/^{39}\text{Ar}$ data of muscovite from the Porsgrunn–Kristiansand Shear Zone (Southern Norway)

Sample number	^{40}Ar ($\times 10^{-15}$ mol)	^{39}Ar ($\times 10^{-17}$ mol)	^{38}Ar ($\times 10^{-18}$ mol)	^{36}Ar ($\times 10^{-18}$ mol)	$^{37}\text{Ar}/^{39}\text{Ar}$	$^{40}\text{Ar}^*/^{39}\text{Ar}$	% $^{40}\text{Ar}^*$	Date (Ma) ($\pm 2\sigma$)
<i>Low-Al muscovite</i>								
1	10.8375 \pm 0.0128	11.818 \pm 0.082	2.22 \pm 0.76	1.20 \pm 0.19	–	88.637	96.7	880.3 \pm 13.2
2	9.7142 \pm 0.0090	10.600 \pm 0.056	1.83 \pm 0.82	0.62 \pm 0.16	–	89.838	98.1	889.8 \pm 11.1
3	9.3697 \pm 0.0095	10.283 \pm 0.057	2.73 \pm 1.20	0.24 \pm 0.18	–	90.350	99.2	893.8 \pm 11.8
4	9.6828 \pm 0.0172	10.520 \pm 0.075	1.99 \pm 1.11	0.61 \pm 0.18	–	90.245	98.1	892.9 \pm 13.7
5	9.3084 \pm 0.0131	10.405 \pm 0.062	1.56 \pm 0.74	–0.01 \pm 0.19	–	89.642	100.0	888.2 \pm 12.6
6	7.0948 \pm 0.0120	7.860 \pm 0.071	1.25 \pm 0.99	0.23 \pm 0.17	–	89.322	99.0	885.7 \pm 17.0
7	9.7398 \pm 0.0096	10.460 \pm 0.059	2.38 \pm 0.97	1.00 \pm 0.19	–	90.213	97.0	892.7 \pm 12.3
8	7.2216 \pm 0.0103	7.968 \pm 0.046	2.72 \pm 1.12	0.55 \pm 0.20	–	88.513	97.7	879.4 \pm 15.0
9	8.9495 \pm 0.0098	9.744 \pm 0.049	3.05 \pm 1.33	0.85 \pm 0.19	–	89.211	97.2	884.8 \pm 12.1
10	8.9298 \pm 0.0135	9.545 \pm 0.057	3.94 \pm 1.24	1.06 \pm 0.19	–	90.215	96.5	892.7 \pm 13.3
11	8.3889 \pm 0.0098	9.107 \pm 0.079	2.76 \pm 1.01	0.95 \pm 0.22	–	88.971	96.7	883.0 \pm 17.2
$J = 0.00710$								
<i>High-Al muscovite fish</i>								
12	6.2628 \pm 0.0181	6.360 \pm 0.058	1.29 \pm 1.06	2.04 \pm 0.24	–	88.929	90.4	882.6 \pm 23.6
13	10.5153 \pm 0.0244	10.962 \pm 0.071	3.12 \pm 1.07	2.21 \pm 0.27	–	89.895	93.8	890.2 \pm 15.8
14	7.1680 \pm 0.0139	7.438 \pm 0.096	1.44 \pm 1.14	2.42 \pm 0.20	1.812	86.932	90.2	866.9 \pm 24.8
15	6.7699 \pm 0.0138	7.090 \pm 0.068	1.68 \pm 0.73	1.57 \pm 0.17	–	88.862	93.1	882.1 \pm 18.9
16	7.8086 \pm 0.0237	8.125 \pm 0.065	1.95 \pm 1.25	1.65 \pm 0.20	–	90.019	93.7	891.2 \pm 17.6
17	6.5907 \pm 0.0136	7.134 \pm 0.076	1.00 \pm 0.69	1.08 \pm 0.19	–	87.832	95.1	874.0 \pm 20.5
18	13.3154 \pm 0.0205	14.123 \pm 0.090	3.13 \pm 1.18	2.32 \pm 0.21	–	89.353	94.8	886.0 \pm 12.3
19	10.5541 \pm 0.0142	11.365 \pm 0.078	2.32 \pm 0.91	2.41 \pm 0.21	–	86.522	93.2	863.6 \pm 14.0
20	8.0405 \pm 0.0137	8.563 \pm 0.069	2.75 \pm 1.12	1.79 \pm 0.21	6.649	88.561	94.0	879.7 \pm 18.1
21	6.3906 \pm 0.0127	6.956 \pm 0.068	0.69 \pm 1.07	0.74 \pm 0.20	–	88.639	96.6	880.4 \pm 20.0
$J = 0.00710$								
<i>Composite muscovite fish</i>								
22	9.3675 \pm 0.0105	10.051 \pm 0.100	–0.14 \pm 0.82	0.78 \pm 0.18	–	90.818	97.5	897.4 \pm 17.0
23	10.7439 \pm 0.0191	11.441 \pm 0.089	2.92 \pm 0.76	2.40 \pm 0.21	3.625	88.144	93.7	876.5 \pm 16.2
24	10.4434 \pm 0.0210	11.050 \pm 0.072	2.77 \pm 0.93	2.41 \pm 0.21	3.229	88.436	93.4	878.8 \pm 15.3
25	6.8752 \pm 0.0105	7.227 \pm 0.073	2.40 \pm 1.01	1.00 \pm 0.20	–	90.980	95.7	898.7 \pm 20.1
26	5.9800 \pm 0.0104	6.563 \pm 0.069	1.92 \pm 0.93	1.21 \pm 0.19	5.660	86.352	94.5	862.3 \pm 24.2
27	5.8897 \pm 0.0134	6.284 \pm 0.056	1.98 \pm 1.19	1.44 \pm 0.20	–	86.877	92.8	866.5 \pm 20.5
28	7.5450 \pm 0.0095	8.030 \pm 0.060	2.26 \pm 0.88	1.42 \pm 0.20	–	88.659	94.4	880.5 \pm 16.7
29	7.9595 \pm 0.0172	8.581 \pm 0.085	1.57 \pm 1.16	1.42 \pm 0.19	–	87.785	94.7	873.6 \pm 18.3
30	10.8991 \pm 0.0178	11.695 \pm 0.062	1.13 \pm 0.98	0.28 \pm 0.16	–	92.415	99.2	909.8 \pm 10.7
31	7.2496 \pm 0.0118	7.925 \pm 0.060	0.70 \pm 1.12	0.30 \pm 0.19	–	90.298	98.8	893.3 \pm 16.2
$J = 0.00710$								

Typical laser blank values are $^{40}\text{Ar} = 4.67 \times 10^{-16}$, $^{39}\text{Ar} = 2.90 \times 10^{-18}$, $^{38}\text{Ar} = 3.25 \times 10^{-18}$, $^{37}\text{Ar} = 1.49 \times 10^{-17}$ and $^{36}\text{Ar} = 6.24 \times 10^{-18}$ moles. Data corrected for system blanks, radioactive decay subsequent to irradiation, mass discrimination, and interfering K-, Ca-, and Cl-derived isotopes of argon. Errors do not include the error in the irradiation parameter, J . The analytical procedures follow those outlined by Mulch *et al.* (2002b).

various stages of this study, and F. Bussy for help with LA-ICP-MS. We acknowledge the perceptive and constructive reviews by J. K. W. Lee, S. Kelley and S. Smith, which substantially improved the manuscript.

References

- BANOS, J.O., AMOURIC, M., DEFOUQUET, C. & BARONNET, A. 1983. Interlayering and interlayer slip in biotite as seen by HRTEM. *American Mineralogist*, **68**, 754–758.
- BELL, I.A., WILSON, C.J.L., MCLAREN, A.C. & ETHERIDGE, M.A. 1986. Kinks in mica: role of dislocations and (001) cleavage. *Tectonophysics*, **78**, 201–228.
- COSCA, M.A., HUNZIKER, J.C., HUON, S. & MASSON, H. 1992. Radiometric age constraints on mineral growth, metamorphism and tectonism of the Gummfluh Klippe, Briançonnais domain of the Prealps, Switzerland. *Contributions to Mineralogy and Petrology*, **112**(4), 439–449.
- COSTA, S. & MALUSKI, H. 1988. Use of $^{40}\text{Ar}/^{39}\text{Ar}$ stepwise heating method for dating mylonite zones: an example of the St. Bartélémy Massif (Northern Pyrenees, France). *Chemical Geology*, **72**, 127–144.
- CHRISTENSEN, J.N., ROSENFELD, J.L. & DEPAOLO, D.J. 1988. Rates of tectonometamorphic processes from rubidium and strontium isotopes in garnet. *Science*, **244**, 1465–1469.
- DODSON, M.H. 1973. Closure temperature in cooling geochronological systems. *Contributions to Mineralogy and Petrology*, **40**, 259–274.
- DUNLAP, W.J. 1997. Neocrystallization or cooling? $^{40}\text{Ar}/^{39}\text{Ar}$ ages of white micas from low-grade mylonites. *Chemical Geology*, **143**, 181–203.
- DUNLAP, W.J., TEYSSIER, C., MCDUGALL, I. & BALDWIN, S. 1991. Ages of deformation from K/Ar and $^{40}\text{Ar}/^{39}\text{Ar}$ dating of white micas. *Geology*, **19**, 1213–1216.
- ETHERIDGE, M.A. & HOBBS, B.E. 1974. Chemical and deformational controls on recrystallization of mica. *Contributions to Mineralogy and Petrology*, **43**, 111–124.
- FREEMAN, S.R., INGER, S., BUTLER, R.W.H. & CLIFF, R.A. 1997. Dating deformation using Rb–Sr in white mica: greenschist facies deformation ages from the Entrelor shear zone, Italian Alps. *Tectonics*, **16**, 57–76.
- GETTY, S.R. & GROMET, L.P. 1992. Geochronological constraints on ductile deformation, crustal extension, and doming about a basement–cover boundary, New England, Appalachians. *American Journal of Science*, **292**, 359–397.
- GILETTI, B.J. 1974. Studies in diffusion I: Argon in phlogopite mica. In: HOFMANN, A.W., GILETTI, B.J., YODER, H.S. & YUND, R.A. (eds) *Geochemical Transport and Kinetics*. Publications of the Carnegie Institution of Washington, **634**, 107–115.
- GIORGIS, D., COSCA, M.A. & LI, S. 2000. Distribution and significance of extraneous argon in UHP eclogite (Sulu terrain, China): insights from in situ $^{40}\text{Ar}/^{39}\text{Ar}$ UV-laser ablation analysis. *Earth and Planetary Science Letters*, **181**, 605–615.
- GOODWIN, L.B. & RENNE, P.R. 1991. Effects of progressive mylonitization on Ar retention in biotites from the Santa Rosa mylonite zone (California), and thermochronologic implications. *Contributions to Mineralogy and Petrology*, **108**, 283–297.
- GOODWIN, L.B. & WENK, H.R. 1990. Intracrystalline folding and cataclasis in biotite of the Santa Rosa mylonite zone: HVEM and TEM observations. *Tectonophysics*, **172**, 201–214.
- GUIDOTTI, C.V. 1986. Micas in metamorphic rocks. In: BAILEY, S.W. (ed.) *Micas*. Mineralogical Society of America, Reviews in Mineralogy, **13**, 357–467.
- HAMES, W.E. & BOWRING, S.A. 1994. An empirical evaluation of the argon diffusion

- geometry in muscovite. *Earth and Planetary Science Letters*, **124**, 161–167.
- HAMES, W.E. & CHENEY, J.T. 1997. On the loss of $^{40}\text{Ar}^*$ from muscovite during polymetamorphism. *Geochimica et Cosmochimica Acta*, **61**, 3863–3872.
- HANDY, M.R. 1987. The structure, age, and kinematics of the Pogallo fault zone, Southern Alps, northwestern Italy. *Eclogae Geologicae Helveticae*, **80**, 593–632.
- HANDY, M.R. & ZINGG, A. 1991. The tectonic and rheological evolution of an attenuated cross section of the continental crust: Ivrea crustal section, southern Alps, northwestern Italy and Switzerland. *Geological Society of America Bulletin*, **103**, 236–253.
- HARRISON, T.M., DUNCAN, I. & McDUGALL, I. 1985. Diffusion of ^{40}Ar in biotite: temperature, pressure, and compositional effects. *Geochimica et Cosmochimica Acta*, **49**, 2461–2468.
- HESS, J.C., LIPPOLT, H.J., GURBANOV, A.G. & MICHALSKI, I. 1993. The cooling history of the late Pliocene Eldzhurtinskiy granite (Caucasus, Russia) and the thermochronological potential of grain-size age relationships. *Earth and Planetary Science Letters*, **117**, 393–406.
- HODGES, K.V., HAMES, W.E. & BOWRING, S.A. 1994. $^{40}\text{Ar}/^{39}\text{Ar}$ age gradients in micas from a high-temperature low-pressure metamorphic terrain—evidence for very slow cooling and implications for the interpretation of age spectra. *Geology*, **22**, 55–58.
- JABOYEDOFF, M. & COSCA, M.A. 1999. Dating incipient metamorphism using $^{40}\text{Ar}/^{39}\text{Ar}$ geochronology and XRD modeling: a case study from the Swiss Alps. *Contributions to Mineralogy and Petrology*, **135**, 93–113.
- KELLEY, S.P. 2002. Excess argon in K–Ar and Ar/Ar geochronology. *Chemical Geology*, **188**, 1–22.
- KELLEY, S.P. & WARTH, J.A. 2000. Rapid kimberlite ascent and the significance of Ar/Ar ages in xenolith phlogopites. *Science*, **285**, 609–611.
- KELLEY, S.P., ARNAUD, N.O. & TURNER, S.P. 1994. High-spatial resolution $^{40}\text{Ar}/^{39}\text{Ar}$ investigations using an ultra-violet laser probe extraction technique. *Geochimica et Cosmochimica Acta*, **58**, 3519–3525.
- KIRSCHNER, D.L., COSCA, M.A., MASSON, H. & HUNZIKER, J.C. 1996. Staircase $^{40}\text{Ar}/^{39}\text{Ar}$ spectra of fine-grained white mica: timing and duration of deformation and empirical constraints on argon diffusion. *Geology*, **24**, 747–750.
- KRAMAR, N., COSCA, M.A. & HUNZIKER, J.C. 2001. Heterogeneous $^{40}\text{Ar}^*$ distributions in naturally deformed muscovite: in situ UV-laser ablation evidence for microstructurally controlled intragrain diffusion. *Earth and Planetary Science Letters*, **192**, 377–388.
- KRAMAR, N., COSCA, M.A., BUFFAT, P.A. & BAUMGARTNER, L.P. 2003. Stacking fault-enhanced argon diffusion in naturally deformed muscovite. In: VANCE, D., MÜLLER, W. & VILLA, I. (eds) *Geochronology: Linking the Isotopic Record with Petrology and Textures*. Geological Society, London, Special Publications, **220**, 249–260.
- LEE, J.K.W. 1995. Multipath diffusion in geochronology. *Contributions to Mineralogy and Petrology*, **120**, 60–82.
- LO, C.H. & ONSTOTT, T.C. 1989. ^{39}Ar recoil artifacts in chloritized biotite. *Geochimica et Cosmochimica Acta*, **53**, 2697–2711.
- MARES, V.M. & KRONENBERG, A.K. 1993. Experimental deformation of muscovite. *Journal of Structural Geology*, **15**, 1061–1075.
- MARKLEY, M.J., TEYSSIER, C. & COSCA, M.A. 2002. The relation between grain size and $^{40}\text{Ar}/^{39}\text{Ar}$ date for Alpine white mica from the Siviez–Mischabel Nappe, Switzerland. *Journal of Structural Geology*, **24**, 1937–1955.
- MASUDA, T., MOROKAWA, T., NAKAYAMA, Y. & SUZUKI, S. 1997. Grain-boundary migration of quartz during annealing experiments at high temperatures and pressures with implications for metamorphic geology. *Journal of Metamorphic Geology*, **15**, 311–322.
- McDUGALL, I. & HARRISON, T.M. 1999. *Geochronology and Thermochronology by the $^{40}\text{Ar}/^{39}\text{Ar}$ Method*, 2nd. Oxford University Press, Oxford, **269**.
- MEZGER, K., VANDERPLUIM, B.A., ESSENE, E.J. & HALLIDAY, A.N. 1991. Synorogenic collapse—a perspective from the middle crust, the Proterozoic Grenville orogen. *Science*, **254**(5032), 695–698.
- MORRISON, J. & ANDERSON, J.L. 1998. Footwall refrigeration along a detachment fault: implications for the thermal evolution of core complexes. *Science*, **279**, 63–66.
- MULCH, A., COSCA, M.A. & FIEBIG, J. 2002a. In-situ $^{40}\text{Ar}/^{39}\text{Ar}$ UV laser dating of mylonitic mica fish: cooling or crystallization ages? *Geochimica et Cosmochimica Acta*, **66**, A532.
- MULCH, A., COSCA, M.A. & HANDY, M.R. 2002b. In-situ UV-laser $^{40}\text{Ar}/^{39}\text{Ar}$ geochronology of a micaceous mylonite—an example of defect-enhanced argon loss. *Contributions to Mineralogy and Petrology*, **142**, 738–752.
- MULCH, A., ROSENAU, M.R., DÖRR, W. & HANDY, M.R. 2002c. The age and structure of dikes along the tectonic contact of the Ivrea–Verbano and Strona–Ceneri Zones (southern Alps, Northern Italy, Switzerland). *Swiss Bulletin of Mineralogy and Petrology*, **82**, 55–76.
- MÜLLER, W. 2003. Strengthening the link between geochronology, textures and petrology. *Earth and Planetary Science Letters*, **206**, 237–251.
- MÜLLER, W., AERDEN, D. & HALLIDAY, A.N. 2000a. Isotopic dating of strain fringe increments: duration and rates of deformation in shear zones. *Science*, **288**, 2195–2198.
- MÜLLER, W., MANCKTELOW, N.S. & MEIER, M. 2000b. Rb–Sr microchrons of synkinematic mica in mylonites: an example from the DAV fault of the Eastern Alps. *Earth and Planetary Science Letters*, **180**, 385–397.
- PHILLIPS, D. & ONSTOTT, T.C. 1988. Argon isotope zoning in mantle phlogopite. *Geology*, **16**, 542–546.
- REDDY, S.M., KELLEY, S.P. & WHEELER, J. 1996. A $^{40}\text{Ar}/^{39}\text{Ar}$ laser probe study of micas from the Sesia Zone, Italian Alps: implications for metamorphic and deformation histories. *Journal of Metamorphic Petrology*, **14**, 493–508.
- REDDY, S.M., POTTS, G.J. & KELLEY, S.P. 2001. $^{40}\text{Ar}/^{39}\text{Ar}$ ages in deformed potassium feldspar: evidence of microstructural control on Ar isotope systematics. *Contributions to Mineralogy and Petrology*, **141**, 186–200.
- SCAILLET, S., FÉRAUD, G., LAGABRIELLE, Y., BALLÈVRE, M. & RUFFET, G. 1990. $^{40}\text{Ar}/^{39}\text{Ar}$ laser/probe dating by step-heating and spot fusion of phengites from the Dora Maira nappe of the western Alps. *Geology*, **18**, 741–744.
- SCHMID, S.M. & HANDY, M.R. 1991. Towards a genetic classification of fault rocks: geological usage and tectonophysical implications. In: MÜLLER, D.W., MCKENZIE, J.A. & WEISSERT, H. (eds) *Controversies in Modern Geology*. Academic Press, London, 339–361.
- SHEA, W.T. & KRONENBERG, A.K. 1992. Rheology and deformation mechanisms of an isotropic mica schist. *Journal of Geophysical Research*, **97**, 15201–15237.
- SHERLOCK, S.C. & HETZEL, R. 2001. A laser/probe $^{40}\text{Ar}/^{39}\text{Ar}$ study of pseudotachylite from the Tambach Fault Zone, Kenya: direct isotopic dating of brittle faults. *Journal of Structural Geology*, **23**, 33–44.
- SIBSON, R.H. 1986. Earthquakes and rock deformation in crustal fault zones. *Annual Review of Earth and Planetary Sciences*, **14**, 149–175.
- STÜNTZ, H. 1998. Syndeformational recrystallization—dynamic or compositionally induced? *Contributions to Mineralogy and Petrology*, **131**, 219–236.
- TULLIS, J., SNOKE, A.W. & TODD, V.R. 1982. Significance and petrogenesis of mylonitic rocks. *Geology*, **10**, 227–230.
- VANCE, D. & O'NIANS, R.K. 1990. Isotopic chronometry of zoned garnets—growth-kinetics and metamorphic histories. *Earth and Planetary Science Letters*, **97**, 227–240.
- WEST, D.P. & LUX, D.R. 1993. Dating mylonitic deformation by the $^{40}\text{Ar}/^{39}\text{Ar}$ method: an example from the Norumbega Fault Zone, Maine. *Earth and Planetary Science Letters*, **120**, 221–237.
- WIJBRANS, J.R. & McDUGALL, I. 1986. $^{40}\text{Ar}/^{39}\text{Ar}$ dating of white micas from an alpine high-pressure metamorphic belt on Naxos (Greece)—the resetting of the argon isotopic system. *Contributions to Mineralogy and Petrology*, **93**, 187–194.
- WRIGHT, N., LAYER, P.W. & YORK, D. 1991. New insights into the thermal history from single grain $^{40}\text{Ar}/^{39}\text{Ar}$ analysis of biotite. *Earth and Planetary Science Letters*, **104**, 70–79.
- YUND, R.A. & TULLIS, J. 1991. Compositional changes of minerals associated with dynamic recrystallization. *Contributions to Mineralogy and Petrology*, **108**, 346–355.